NANO LETTERS

Letter

pubs.acs.org/NanoLett

Structure and Electronic Transport in Graphene Wrinkles

Wenjuan Zhu,* Tony Low, Vasili Perebeinos, Ageeth A. Bol, Yu Zhu, Hugen Yan, Jerry Tersoff, and Phaedon Avouris*

IBM Thomas J. Watson Research Center, Yorktown Heights, New York 10598, United States

Supporting Information

ABSTRACT: Wrinkling is a ubiquitous phenomenon in two-dimensional membranes. In particular, in the large-scale growth of graphene on metallic substrates, high densities of wrinkles are commonly observed. Despite their prevalence and potential impact on large-scale graphene electronics, relatively little is known about their structural morphology and electronic properties. Surveying the graphene landscape using atomic force microscopy, we found that wrinkles reach a certain maximum height before folding over. Calculations of the energetics explain the morphological transition and indicate that the tall ripples are collapsed into narrow standing wrinkles by van der Waals forces, analogous to large-diameter nanotubes. Quantum transport calculations show that conductance through these "collapsed wrinkle" structures is limited mainly by a density-of-states bottleneck and by interlayer tunneling across the collapsed bilayer region. Also through systematic measurements across large numbers of devices with wide "folded wrinkles", we find a distinct anisotropy in their electrical resistivity, consistent with our transport simulations. These results highlight the coupling between morphology and electronic properties, which has important practical implications for large-scale high-speed graphene electronics.

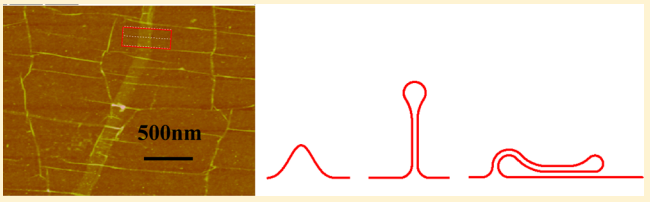

KEYWORDS: *graphene, fold, wrinkle, electronic transport, ripples*

The advance of a new generation of very high speed graphene electronics[1−8] depends upon understanding and controlling the interaction of graphene with the surroundings, especially the supporting substrate.[9−11] Graphene obtained by chemical vapor deposition (CVD) on metals[12−15] is emerging as a powerful platform for graphene electronics with wafer-scale compatible fabrication. However, carrier mobilities in CVD graphene are smaller than for exfoliated graphene,[12−15] and the limiting electron scattering mechanisms in these large-scale graphene wafers are not well understood. Recently, several studies have reported on the polycrystalline nature of CVD graphene and the associated electrical resistances due to grain boundaries,[16−19] which can be significant. Fortunately, improvements in current state-of-the-art growth techniques have led to large micrometer scale grain sizes.[16−18] Hence, in typical submicrometer graphene devices electron scattering mechanisms at length-scale much smaller than the grain size are likely responsible for the inferior carrier mobilities.

A particular issue for CVD graphene is the presence of wrinkles. These are formed by differential thermal expansion, as the metal contracts more than the graphene during postgrowth cooling, leaving an excess area of graphene.[20−24] Wrinkles are still present after transfer to the device substrate, as can be clearly seen in SEM images. Figure 1a shows such an image on a SiO_2/Si substrate. The dark lines correspond to the graphene wrinkles, since these regions reflect fewer secondary electrons. The same features are also reflected in the Raman images. Figure 1b shows the Raman G band intensity map of the same graphene area shown in Figure 1a. It displays the total intensity of the G phonon band. There are clear line features in the phonon spectrum at the same locations as the features in the SEM image. The total G band intensity is higher at the wrinkles due to the extra layers of graphene as compared to the surrounding area.[25] In Figure 1c, we show a map of the ratio of the Raman D to G band intensities. We note that there is no corresponding line feature in the D to G ratio map at the position of the wrinkle, indicating that this feature is not a line defect, such as grain boundary that gives rise to an increased D band.[18,26] A TEM cross-sectional image of such a wide graphene wrinkle is shown in Figure 1d. The width of this wrinkle is about 50 nm. The profile of TEM intensity in the boxed area is shown in the inset. The multilayer structure of the wrinkle clearly shows that it is not a standing wrinkle but a folded structure.[20]

More quantitative information about the wrinkle distribution is obtained using AFM with "SuperSharp" tips. Figure 2a,b shows the AFM images of a wide graphene wrinkle (∼135 nm) and a narrow graphene wrinkle (∼16 nm). The AFM heights of the marked region in panels a and b are shown in Figure 2c and are about 0.9 and 3.8 nm, respectively. Figure 2d gives the statistical distribution of the wrinkle heights as a function of their width. The wide wrinkles all have similar height, roughly 1 nm, but they exhibit a broad range of widths. In contrast, the narrow wrinkles are taller and have a broad distribution of

Received: February 9, 2012
Revised: May 14, 2012
Published: May 30, 2012

   dx.doi.org/10.1021/nl300563h | *Nano Lett.* 2012, 12, 3431−3436

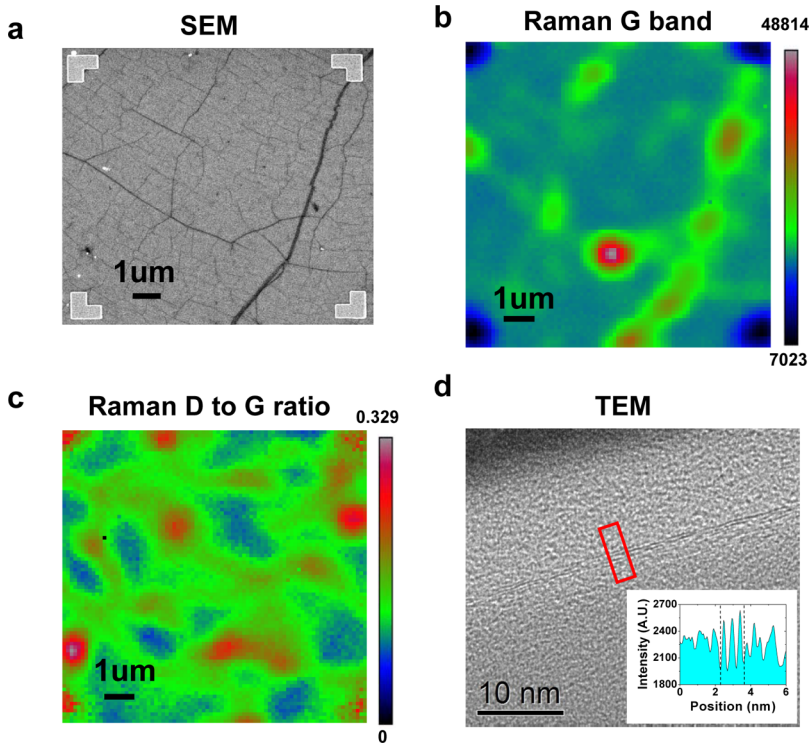

Figure 1. Physical characterization of CVD graphene on SiO_2/Si substrate. (a) SEM image of graphene on a SiO_2/Si substrate. (b) Raman G band intensity map of graphene on SiO_2/Si substrate. (c) Map of the D to G Raman band intensities ratio of graphene on SiO_2/Si substrate. (e) TEM cross-section of graphene on SiO_2/Si substrate. On top of the graphene are PMMA resist and Cr layers. The inset shows the profile of the TEM contrast in the red rectangle area.

heights, ranging roughly from 2 to 6 nm. Their width is apparently below the resolution of our AFM.

Little is known about the factors determining the distribution of wrinkles, which may depend on the details of CVD growth and subsequent transfer. However, previous studies have already yielded insight into the morphology of individual wrinkles. Figure 2e−g shows three distinct morphologies: panel e is the simple ripple geometry usually assumed;[23,27−31] panel g is the recently identified folded geometry;[20] and we propose an intermediate geometry, panel f, a "standing collapsed wrinkle". The sequence of shape is easily understood at the qualitative level, as arising from the competition between elastic bending and van der Waals binding.[20,32] The ripple structure minimizes the bending distortion. However, when there is a large amount of excess material, collapsing it to form bilayers or folding it to form trilayers provides additional van der Waals binding, at the cost of progressively increased bending. For a given structure, the binding increases with length, while the bending energy is constant (roughly proportional to the number of sharp bends), leading to the sequence of shapes.

To better understand the energetic competition and resulting morphologies, we perform total energy calculations, including the van der Waals binding and elastic bending and assuming a variational form for the geometry. The only material parameters are the bending stiffness κ and the van der Waals binding energy β (for details see Supporting Information). We use the value $\kappa = 1.4$ eV[33,34] for the bending stiffness of graphene, and $\beta = 40$ meV per carbon atom[32] for the van der Waals adhesion energy between the graphene sidewalls. When the excess graphene length (i.e., the graphene length compared to the substrate length) is greater than $L_m \approx 24(\kappa/2\beta)^{1/2} \approx 16.3$ nm, we find that the "folded" structure (Figure 2g) has the lowest energy. Below this, the standing collapsed wrinkle (Figure 2f) has lower energy. The height of the "standing wrinkle" at the transition (i.e., the maximum height) is about 8.4 nm, very close to $L_m/2$. Taking into account the uncertainties in AFM of flexible structures and in the parameters κ and β, this estimate is consistent with the experimental value found above of 5−6 nm.

For electronic devices, the most important issue for graphene wrinkles is their impact on transport. Here we address this both experimentally and theoretically. For "folded wrinkles", we systematically measured the electrical resistivities both along the fold and across it, using four-probe devices as illustrated in Figure 3a,b. Their averaged resistances, herein denoted as $\langle R_{al} \rangle$ and $\langle R_{ac} \rangle$, respectively, are plotted in Figure 3c,d as functions of the gate voltage V_g and compared with resistances of the control (flat) devices $\langle R_0 \rangle$. The resistances involving the fold structure exhibit an interesting anisotropy: (i) $\langle R_{al} \rangle$ is smaller than $\langle R_0 \rangle$, especially when biased near the charge neutrality point. (ii) $\langle R_{ac} \rangle$ shows no difference from $\langle R_0 \rangle$ within error. We cannot directly measure the resistance of standing wrinkles, because their high density precludes contacting them individually. Hence, each device with the folded wrinkles has a control device constructed beside it, which measures the resistances associated with these smaller background wrinkles. $\langle R_{al} \rangle$, $\langle R_{ac} \rangle$, and $\langle R_0 \rangle$ are obtained by averaging over dozens of these devices.

In general, folds could trap impurities that act as dopants or scatterers, affecting the resistance. Such extrinsic effects would depend on the details of processing. Our measurements suggest that trapped impurities are not a significant factor here, see Supporting Information. We therefore address theoretically the intrinsic resistance of folds, without any such impurities or defects. Electrical transport along folded wrinkles can be

dx.doi.org/10.1021/nl300563h | Nano Lett. 2012, 12, 3431−3436

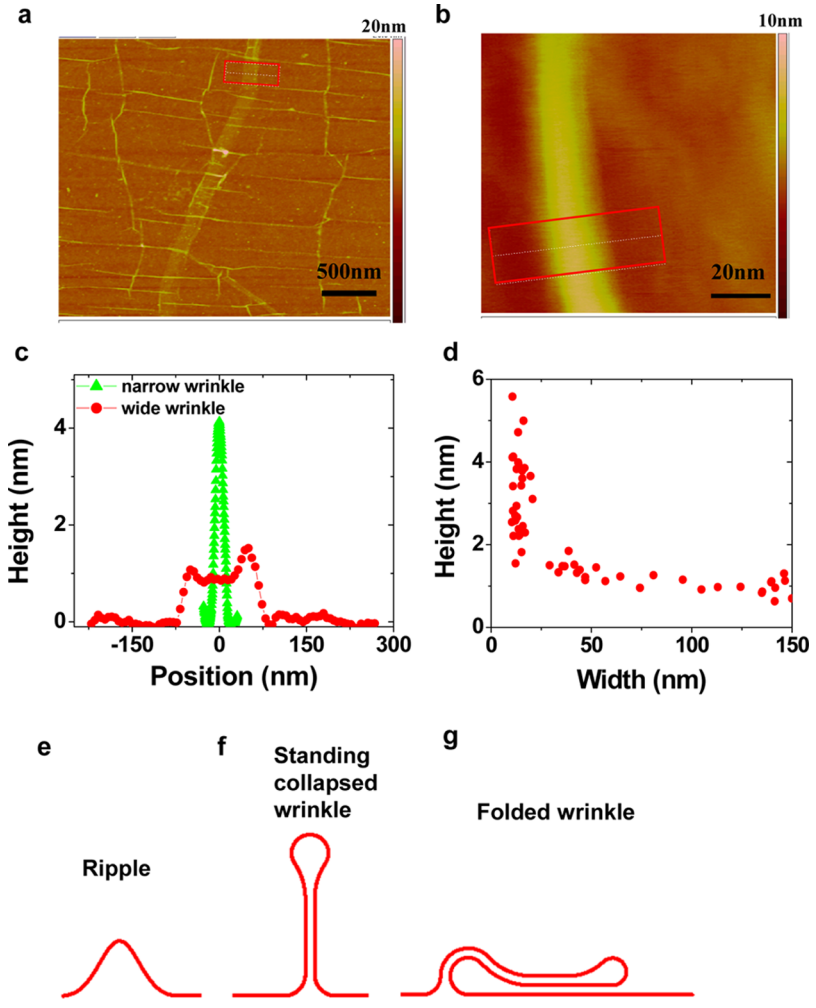

Figure 2. Wrinkle topographies and structures. (a) AFM image of graphene on SiO_2/Si substrate. The field of view is 3 μm. (b) AFM image of a narrow wrinkle. Field of view is 100 nm. (c) The step profile of a wide and a narrow wrinkle. (d) Statistical distribution of wrinkle heights as a function of their width. Schematic illustration of three classes of graphene wrinkles: (e) simple ripple; (f) standing collapsed wrinkle; (g) folded wrinkle. For details on these geometries see the Supporting Information.

analyzed using a simple diffusive transport model. Roughly speaking, the folded wrinkle can be viewed as a strip of trilayer graphene. Neglecting hybridization between layers, the electrostatic problem for the trilayer can be solved self-consistently. The resulting carrier distributions within each layer are plotted in Figure 4a. Due to nonlinear charge screening,[35] the carriers are almost all confined to the bottom layer for large V_g, while the carriers are more equally distributed when the device is biased near the charge neutrality point. The transport coefficient (i.e., the mobility) is commonly seen to improve with decreasing carrier density,[10,36,37] and we confirm this behavior in our own devices (see Supporting Information Section 6). Therefore the charge redistribution in the trilayer structure should improve its effective carrier mobility relative to that of monolayer graphene at a given electrostatic doping. We confirm this by quantitatively modeling the experiments as shown in Figure 4b (see Supporting InformationSection 3). The largest difference in electrical resistance between $\langle R_{al} \rangle$ and $\langle R_0 \rangle$ occurs at the charge neutrality point, when charge redistribution in the trilayer graphene is most effective.

Electrical transport across folded wrinkles, however, cannot be explained with the simple diffusive model above. The excess length associated with the fold and its reduced doping would both increase the resistance. If this were the controlling physics, the resistance would be an order larger than what is experimentally observed, see Figure 4c. This discrepancy can be reconciled by taking into account an additional conduction pathway via interlayer tunneling[38,39] across the collapsed bilayer graphene, which can reduce the larger resistance associated with the density-of-states bottleneck.

To estimate the role of interlayer tunneling in limiting the resistance, we performed quantum transport simulations based on the nonequilibrium Green's function method.[40] Since we are also interested in the resistance of standing wrinkles, we perform calculations for the simpler geometry of Figure 2f, but for varying excess graphene lengths spanning the range from standing to folded geometries. For both geometries, we expect reduced doping in the raised graphene areas, reflecting the poor coupling to the gate due to its geometry for the standing wrinkle or due to screening by the bottom graphene layer for the folded wrinkle. For simplicity, we treat these regions as undoped, giving an upper bound on the resistance. The resulting room-temperature resistances are shown in Figure 5a as a function of the length λ of the collapsed bilayer region. Depending on the orientation of the wrinkle, the bilayer could have some rotated alignment, but we focus on the simpler case

dx.doi.org/10.1021/nl300563h | *Nano Lett.* 2012, 12, 3431−3436

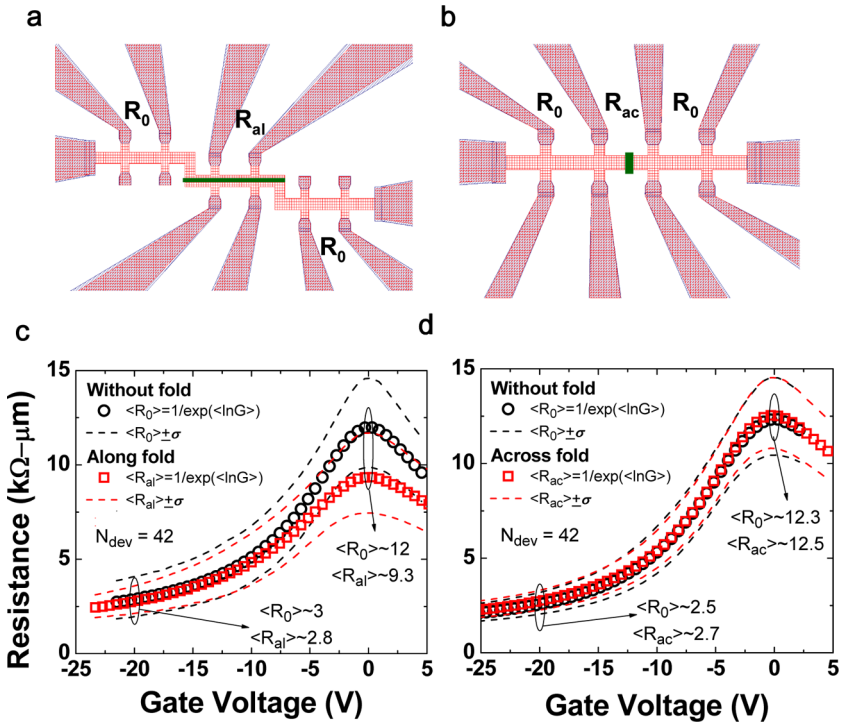

Figure 3. Transport measurements along/across folded wrinkles. (a,b) Device layout of the Hall-bars structures across and along the fold. Control devices without fold are fabricated alongside. (c) Averaged resistances $\langle R_{al}\rangle$ as a function of gate voltage V_g for devices along the fold, compared with control devices $\langle R_0\rangle$. Statistical averages are obtained using the geometric mean sampled over 42 devices. Dashed lines indicate the statistical standard deviations. (d) Same as (c), but for devices measured across the fold $\langle R_{ac}\rangle$. Device length is 2 μm and width is about 0.35 μm (along the fold) and 0.3 μm (across the fold). The fold's width in these devices was 0.14 μm.

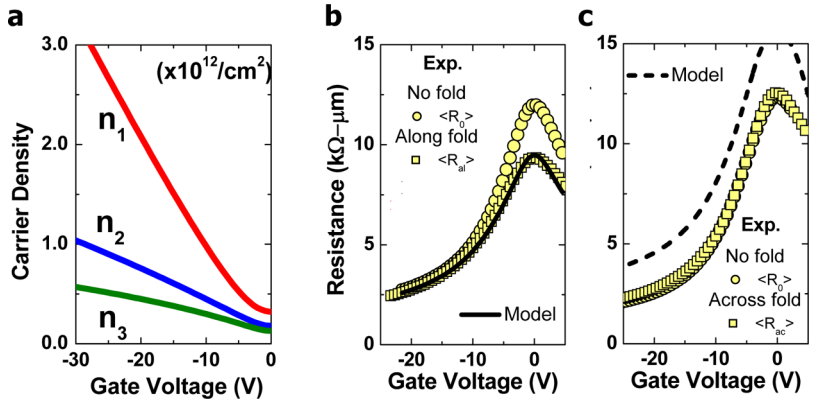

Figure 4. Electrostatics and diffusive transport in graphene fold. (a) Electrostatic modeling of the carrier distribution in a trilayer graphene system, $n_{1,2,3}$, as function of V_g. n_1 is the layer closest to the gate. Finite electron–hole puddles densities of 6.5×10^{11} cm^{-2} is deduced from Hall measurement. (b,c) Modeling of resistance (b) $\langle R_{al}\rangle$ along the fold, and (c) $\langle R_{ac}\rangle$ across the fold, as function of V_g, using a diffusive model as described in the main text (see also Supporting Information). The diffusive model works well for $\langle R_{al}\rangle$ but fails to capture the behavior of $\langle R_{ac}\rangle$.

with zero misorientation, where the stacking depends only on sliding of one layer over the other. We show the average resistance and range for different bilayer alignment.

The most striking feature of Figure 5a is that the resistance depends only very weakly on the excess graphene length. The reason is seen in Figure 5b, which shows that much of the current flows between graphene layers at the base of the wrinkle, rather than flowing through the whole length. To verify this interpretation, we repeat the calculations with the graphene sheet cut at the top of the wrinkle. Despite totally blocking the direct intralayer pathway, the change in resistance is minor. We expect the interlayer transport to be similar for folded wrinkles, since it occurs largely near the base. Thus, our calculations suggest a resistance on the order of ~200 Ω·μm, which is relatively independent of λ, for either type of wrinkles. The resistance observed in our experiments is also very small, below the experimental accuracy, consistent with the small calculated value.

In conclusion, we reported experimental and theoretical measurements of collapsed graphene wrinkles, and compared these. The calculated energetics based on competition between the elastic and van der Waals energies is consistent with the experimental observation of a maximum wrinkle height of ~6 nm, substantiating our physical picture of the structure of standing and folded wrinkles. Our transport experiments on these folded wrinkles yield a distinctive anisotropy in the fold

dx.doi.org/10.1021/nl300563h | Nano Lett. 2012, 12, 3431–3436

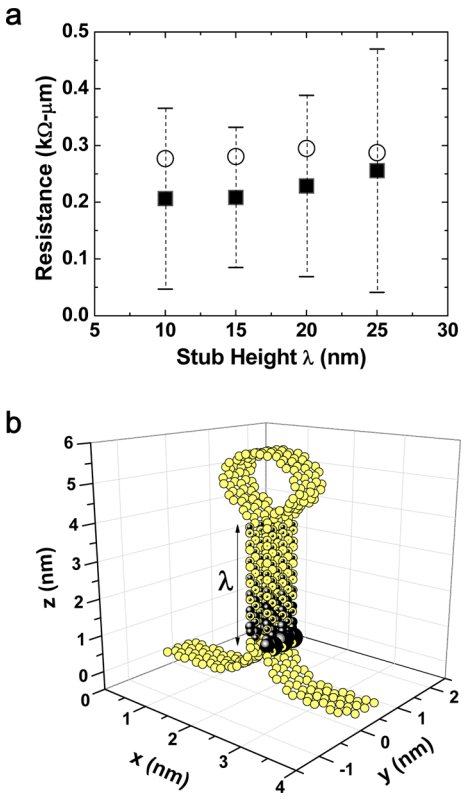

Figure 5. Quantum transport modeling across a collapsed wrinkle. (a) Quantum transport modeling of the room-temperature resistance of the standing collapsed graphene wrinkle as function of the length of the collapsed bilayer λ, averaged over 20 samples with different bilayer stacking alignment (Solid square symbol, with standard deviations indicated). For comparison, open circles show similar calculations where we cut the top of the wrinkle to suppress purely intralayer current. We use the nonequilibrium Green's function method. Details of the method and calculations are described in Supporting Information. (b) Atomic structure and interlayer tunneling for a standing collapsed graphene wrinkle. Bubble plot shows the out-of-plane current density with the bubbles' radius being proportional to the magnitude of current density.

resistivity consistent with our model. We conclude that this anisotropy arises because transport along and across the folded wrinkles are limited by different transport effects: diffusive transport of the charge distributed across the multilayered folds, versus local interlayer tunneling across the collapsed region. From an applications standpoint, the former degrades the on–off ratio, while the latter can contribute a significant resistance to the overall device, of the same order as typical graphene contact resistances.[41,42] Our study therefore identifies a source of electrical performance degradation in CVD grown graphene, and highlights the subtle interplay between morphology and electronic properties. It also underscores the importance of a better fundamental understanding of the formation and engineering of wrinkles.

Methods. The method we used in this work to prepare monolayers of graphene is based on CVD of graphene on Cu and is similar to the method described in ref 13. A Cu foil (25 μm thick, 99.98%, Alfa-Aesar) was placed in a 1 in. diameter quartz furnace tube at low pressure (10^{-6} Torr). After evacuation, the Cu foil was heated to 1050 °C in vacuum. At this temperature, the sample was exposed to ethylene (6 sccm, 6 mTorr) for 10 min. The sample was then cooled down under vacuum. PMMA resist was spin-coated on top of the graphene layer formed on one side of the Cu foil. The Cu foil was then dissolved in 1 M iron chloride. The remaining graphene/PMMA layer was washed with DI water, 1 M HCl, and DI water and transferred to the Si/SiO_2 substrate. Subsequently, the PMMA was dissolved in hot acetone (80 °C) for one hour. The substrate with the transferred graphene was then rinsed with methanol and dried in a stream of nitrogen.

Subsequently, metal alignment marks were formed by lift-off and graphene Hall-bar structures were fabricated by photoresist patterning and O_2 plasma etching. Following that, SEM, AFM, and Raman characterization was performed, and then source/drain and sensing terminals were formed using Ti/Pd/Au metallization and lift-off. The SEM measurements were obtained at 3 KV. The Raman G band intensity is summed in the frequency range of 1480 to 1700 cm^{-1} and the D band intensity is summed in the frequency range of 1253 to 1450 cm^{-1}. The AFM images were taken in the tapping mode with "SuperSharp" silicon tip. The tip radius is less than 5 nm. For TEM analysis, the sample was prepared using dual-beam focus ion beam and imaged in a JEOL 3000F TEM operated at 300 eV.

■ ASSOCIATED CONTENT

Supporting Information

Additional information and figures. This material is available free of charge via the Internet at http://pubs.acs.org.

■ AUTHOR INFORMATION

Notes

The authors declare no competing financial interest.

■ ACKNOWLEDGMENTS

We would like to thank B. Ek, J. Bucchignano, and G. P. Wright for their contributions to device fabrication. We would also like to thank X. Li, M. Freitag, F. Xia, Y. Wu, D. Farmer, Y.-M. Lin, G. Tulevski, and C. Y. Sung for their insightful discussion and help in the project. T. Low gratefully acknowledges use of a computing cluster provided for by Network for Computational Nanotechnology, and partial funding from INDEX-NRI. The authors would also like to thank DARPA for partial financial support through the CERA program.

■ REFERENCES

(1) Meric, I.; et al. Current saturation in zero-bandgap, top-gated graphene field-effect transistors. *Nat. Nanotechnol.* **2008**, *3*, 654–659.
(2) Moon, J. S.; et al. Epitaxial-Graphene RF Field-Effect Transistors on Si-Face 6H-SiC Substrates. *IEEE Electron Device Lett.* **2009**, *30*, 650–652.
(3) Eddy, C. R.; Gaskill, D. K. Silicon Carbide as a Platform for Power Electronics. *Science* **2009**, *324*, 1398–1400.
(4) Wang, H.; Hsu, A.; Wu, J.; Jing, K.; Palacios, T. Graphene-Based Ambipolar RF Mixers. *IEEE Electron Device Lett.* **2010**, *31*, 906–908.
(5) Lin, Y.-M.; et al. 100-GHz Transistors from Wafer-Scale Epitaxial Graphene. *Science* **2010**, *327*, 662.
(6) Liao, L.; et al. High-speed graphene transistors with a self-aligned nanowire gate. *Nature* **2010**, *467*, 305–308.
(7) Wu, Y.; et al. High-frequency, scaled graphene transistors on diamond-like carbon. *Nature* **2011**, *472*, 74–78.
(8) Han, S.-J.; et al. High-Frequency Graphene Voltage Amplifier. *Nano Lett.* **2011**, *11*, 3690–3693.
(9) Chen, J. H.; et al. Charged-impurity scattering in graphene. *Nat. Phys.* **2008**, *4*, 377–381.

(10) Du, X.; Skachko, I.; Barker, A.; Andrei, E. Y. Approaching ballistic transport in suspended graphene. *Nat. Nanotechnol.* **2008**, *3*, 491−495.
(11) Dean, C. R.; et al. Boron nitride substrates for high-quality graphene electronics. *Nat. Nanotechnol.* **2010**, *5*, 722−726.
(12) Li, X.; et al. Large-Area Synthesis of High-Quality and Uniform Graphene Films on Copper Foils. *Science* **2009**, *324*, 1312−1314.
(13) Bae, S.; et al. Roll-to-roll production of 30-in. graphene films for transparent electrodes. *Nat. Nanotechnol.* **2010**, *5*, 574−578.
(14) Kim, K. S.; et al. Large-scale pattern growth of graphene films for stretchable transparent electrodes. *Nature* **2009**, *457*, 706−710.
(15) Lee, S.; Lee, K.; Zhong, Z. Wafer Scale Homogeneous Bilayer Graphene Films by Chemical Vapor Deposition. *Nano Lett.* **2010**, *10*, 4702−4707.
(16) Huang, P. Y. Grains and grain boundaries in single-layer graphene atomic patchwork quilts. *Nature* **2011**, *469*, 389.
(17) Li, X.; et al. Graphene Films with Large Domain Size by a Two-Step Chemical Vapor Deposition Process. *Nano Lett.* **2010**, *10*, 4328−4334.
(18) Yu, Q.; et al. Control and characterization of individual grains and grain boundaries in graphene grown by chemical vapour deposition. *Nat. Mater.* **2011**, *10*, 443−449.
(19) Lahiri, J.; Lin, Y.; Bozkurt, P.; Oleynik, I. I.; Batzill, M. An extended defect in graphene as a metallic wire. *Nat. Nanotechnol.* **2010**, *5*, 326−329.
(20) Kim, K.; et al. Multiply folded graphene. *Phys. Rev. B* **2011**, *83*, 245433.
(21) Hattab, H. Interplay of Wrinkles, Strain, and Lattice Parameter in Graphene on Iridium. *Nano Lett.* **2012**, *12* (2), 678−682.
(22) Paronyan, T. M.; Pigos, E. M.; Chen, G.; Harutyunyan, A. R. Formation of Ripples in Graphene as a Result of Interfacial Instabilities. *ACS Nano* **2011**, *5*, 9619−9627.
(23) Zhang, Y.; et al. Defect-like Structures of Graphene on Copper Foils for Strain Relief Investigated by High-Resolution Scanning Tunneling Microscopy. *ACS Nano* **2011**, *5*, 4014−4022.
(24) Chae, S. J.; et al. Synthesis of Large-Area Graphene Layers on Poly-Nickel Substrate by Chemical Vapor Deposition: Wrinkle Formation. *Adv. Mater.* **2009**, *21*, 2328−2333.
(25) Koh, Y. K.; Bae, M.-H.; Cahill, D. G.; Pop, E. Reliably Counting Atomic Planes of Few-Layer Graphene ($n > 4$). *ACS Nano* **2011**, *5*, 269−274.
(26) Ferrari, A. C. Raman spectroscopy of graphene and graphite: Disorder, electron-phonon coupling, doping and nonadiabatic effects. *Solid State Commun.* **2007**, *143*, 47−57.
(27) Fasolino, A.; Los, J. H.; Katsnelson, M. I. Intrinsic ripples in graphene. *Nat. Mater.* **2007**, *6*, 858−861.
(28) Guinea, F.; Katsnelson, M. I.; Vozmediano, M. A. H. Midgap states and charge inhomogeneities in corrugated graphene. *Phys. Rev. B* **2008**, *77*, 075422.
(29) Katsnelson, M. I.; Geim, A. K. Electron scattering on microscopic corrugations in graphene. *Philos. Trans. R. Soc. London, Ser. A* **2008**, *366*, 195−204.
(30) Vázquez de Parga, A. L.; et al. Periodically Rippled Graphene: Growth and Spatially Resolved Electronic Structure. *Phys. Rev. Lett.* **2008**, *100*, 056807.
(31) Guinea, F.; Horovitz, B.; Le Doussal, P. Gauge fields, ripples and wrinkles in graphene layers. *Solid State Commun.* **2009**, *149*, 1140−1143.
(32) Chopra, N. G.; et al. Fully Collapsed Carbon Nanotubes. *Nature* **1995**, *377*, 135−138.
(33) Girifalco, L. A.; Lad, R. A. Energy of cohension, compressibility, and the potential energy functions of the graphite system. *J. Chem. Phys.* **1956**, *25*, 693−697.
(34) Zacharia, R., Ulbricht, H. & Hertel, T. Interlayer cohesive energy of graphite from thermal desorption of polyaromatic hydrocarbons. *Phys. Rev. B 69*, (**2004**).
(35) Kuroda, M. A.; Tersoff, J.; Martyna, G. J. Nonlinear Screening in Multilayer Graphene Systems. *Phys. Rev. Lett.* **2011**, *106*, 116804.
(36) Zhu, W.; Perebeinos, V.; Freitag, M.; Avouris, P. Carrier scattering, mobilities, and electrostatic potential in monolayer, bilayer, and trilayer graphene. *Phys. Rev. B* **2009**, *80*, 235402.
(37) Lin, Y.-M.; et al. Multicarrier transport in epitaxial multilayer graphene. *Appl. Phys. Lett.* **2010**, *97*, 112107−112103.
(38) Bistritzer, R.; MacDonald, A. H. Transport between twisted graphene layers. *Phys. Rev. B* **2010**, *81*, 245412.
(39) Uryu, S.; Ando, T. Electronic intertube transfer in double-wall carbon nanotubes. *Phys. Rev. B* **2005**, *72*, 245403.
(40) Datta, S. *Electronic transport in mesoscopic systems*; Cambridge University Press: New York, 1997.
(41) Berdebes, D.; Low, T.; Yang, S.; Appenzeller, J.; Lundstrom, M. S. Substrate Gating of Contact Resistance in Graphene Transistors. *IEEE Trans. Electron Device* **2011**, *58*, 3925−3932.
(42) Xia, F.; Perebeinos, V.; Lin, Y.-m.; Wu, Y.; Avouris, P. The origins and limits of metal-graphene junction resistance. *Nat. Nanotechnol.* **2011**, *6*, 179−184.